Elucidating the molecular mechanism of phytochemicals against Parkinson's disease through an integrated systems biology and molecular modeling approach

[#]Ratul Bhowmik[1,2], [#]Sunil Kumar[3], Ajay Manaithiya[1], C. Gopi Mohan[2]*, Bijo Mathew[3]*, Seppo Parkkila[1,4], and Ashok Aspatwar[1]*

[1]Faculty of Medicine and Health Technology, Tampere University, Tampere, Finland.

[2]Bioinformatics and Computational Biology Lab, Amrita School for Nanosciences and Molecular Medicine, Amrita Vishwa Vidyapeetham, Kochi, Kerala State, 682 041, India

[3] Department of Pharmaceutical Chemistry, Amrita School of Pharmacy, Amrita Vishwa Vidyapeetham, AIMS Health Sciences Campus, Kochi 682041, India

[4]Fimlab, Ltd. and TAYS Cancer Centre, Tampere University Hospital, Tampere, Finland.

Abstract

Traditional medicinal plants *Mitragyna Speciosa* and *Plumbago Indica* have exhibited several neuroprotective activities against Parkinson's disease (PD) in several research studies. Nevertheless, further elucidation is needed about the molecular mechanism by which these medicinal plants exert their neuroprotective effects, as well as the relationship between their active constituents' structure and activity. Using a polypharmacology approach, the study identified metabolic pathways targeted by active phytochemicals of these medicinal plants. Extensive system biology approaches, including protein-protein interaction network analysis, KEGG pathway analysis, and gene functional enrichment study, pinpointed that AKT1 was the key gene involved in the molecular mechanism actions of the active phytochemicals concerning neuroprotective actions. A robust machine-learning guided bioactivity prediction model-based web application (https://akt1pred.streamlit.app/) against AKT1 was developed by implementing PubChem and Substructure fingerprint molecular signatures. Further validation of the model was done by conducting ROC and applicability domain analysis, with subsequent molecular docking studies to understand the molecular mechanisms of the phytochemicals. The web application predicted that delphinidin and kaempferol were the most active phytochemicals responsible for the neuroprotective effects of the medicinal plants, which was further supported by extensive molecular docking and molecular dynamics simulation study. These findings indicate a correlation between the structure of these compounds and their bioactivity, with some phytochemicals performing comparably or better than known FDA drugs. Results suggest significant potential for natural products in therapeutic applications, urging further in vitro and in vivo investigation and offering a robust foundation for future research into natural product-based small molecule binding and drug discovery in PD.

Keywords: Network Pharmacology, System Biology, Machine Learning-Assisted QSAR Modeling, Web Application, Molecular Docking, Molecular Dynamic.

***Corresponding Authors**

Ashok Aspatwar ashok.aspatwar@tuni.fi
Bijo Mathew: bijomathew@aims.amrita.edu or bijovilaventgu@gmail.com
C. Gopi Mohan: cgmohan@acnsmm.aims.amrita.edu or cgopi1966@gmail.com

[#] These authors contributed equally to this work.

Heighlights

- Mitragyna Speciosa and Plumbago Indica share certain neuroprotective qualities.
- We determined metabolomics pathways by active plant-based constituents using the polypharmacology technique.
- The development of a reliable stable machine-learning model and a web application
- Web-based application predicted neuroprotective effects of delphinidin and kaempferol

1. Introduction

Idiopathic paralysis agitans, often known as Parkinson's disease (PD), is a prevalent chronic degenerative condition that affects the central nervous system [1]. Muscle stiffness, tremors, dyskinesias, and abnormalities in posture and movement are the main clinical symptoms of PD. Eating and dressing normally are disturbed in extreme circumstances of the disease [2,3]. In PD patients, the number of transmitters in striatal dopaminergic neurons has dramatically decreased, and dopaminergic neurons in the substantia nigra pars compacta are degenerating [4,5]. Movement issues are caused by increased cholinergic neuron activity and decreased nigrostriatal dopaminergic neuron activity. Although the exact origin of PD is still unknown, aberrant -synuclein aggregation, increased oxidative stress, impaired mitochondrial function, and increased neuroinflammation have all been demonstrated to be associated with the death of DA neurons during PD progression [6, 7]. Anti-PD medications typically focus on motor and non-motor symptoms while also offering neuroprotective benefits. Dopamine agonists like pramipexole, ropinirole, rotigotine, and apo-morphine, as well as COMT inhibitors and MAO-B inhibitors like selegiline, rasagiline, and safinamide, are among the anti-PD medications that are clinically used [8–10]. Levodopa is the anti-PD drug that is most successful at treating motor symptoms. Dopamine agonists are frequently used in combination with levodopa in young children with PD. COMT inhibitors may increase the bioavailability of dopamine in the central nervous

system (CNS) by reducing peripheral dopamine metabolism. Levodopa, dopamine agonists, or both can be used alone or in combination with MAO-B inhibitors. However, these anti-PD drugs may provide relief from either motor or non-motor symptoms without affecting the brain's ability to protect itself. As a result, these medications were unable to prevent or delay the progression of PD. Several anti-PD drugs may also have serious side effects, such as nausea, vomiting, nightmares, insomnia, hallucinations, and serotonergic crisis [11,12]. Therefore, it is crucial to create drugs that effectively treat PD while causing little to no adverse effects and having neuroprotective properties.

Natural substances have a wide range of pharmacological effects and great potential for use in creating new medications. The traditional medicinal plant Mitragyna speciosa (M. speciosa), which belongs to the Rubiaceae family, is native to Malaysia and Thailand and is widely utilized in these two nearby Southeast Asian nations [13–15]. Originally from Southeast Asia, Indonesia, the Philippines, and Yunnan in southern China, Plumbago Indica is a member of the Plumbaginaceae family [16,17]. Both natural compounds are used in the treatment of hypertension, diabetes, hepatoprotection, atherogenicity, inflammation, and neuroprotection. However, when we started the chemical and pharmacological inquiry, the theory and mechanisms behind the biological activities had not yet been fully understood [18–22]. Modern medicinal chemistry research has increasingly turned to lead molecules in natural products with therapeutic properties as well as structural optimization of these compounds. Therefore, due to their exceptional efficacy, several natural product constituents have come to the fore as PD treatments with the continual advancement of technology utilized to isolate and purify monomer components.

The therapeutic components, herbal targets, and important pathways of Mitragyna and Plumbago for the treatment of PD were examined using network pharmacology, bioinformatics, and cheminformatics strategies [23-25]. To develop a mechanistic model for predicting the activity of target phytochemicals, a machine-learning-assisted quantitative structure-activity relationship (ML-QSAR) method was developed. The basic idea behind QSAR is that different structural properties of compounds result in different bioactivities. The molecular mechanism was investigated in this study using the network pharmacology approach. A predicted pIC_{50} for a screened natural component was established using the QSAR technique. The robust ML-QSAR model was further implemented as a Python web application, AKT1-Pred (https://akt1pred.streamlit.app/), which provides a user-friendly interface that can predict the inhibitory activity of small molecules against the top gene AKT1 obtained through our polypharmacology based study. This web application has the advantage of being platform-independent to be accessed via a web browser on any operating system or device. Lastly, the stability of the ligand and protein complex as well as its binding modalities were confirmed by molecular docking and dynamics simulation study.

2. Result and Discussion

2.1.Network pharmacology analysis

2.1.1. Chemical compounds and targets acquisition

Seven compounds from mitragyana and two from plumbago plants were screened from the IMPPAT and KNapSAcK databases using OB (30%), likelihood for target (0.1), and DL (0.18) as thresholds. Mitragyana and plumbago, which total 309 and 203 chemical targets, respectively, were found by Swiss Target Prediction. Target discovered 8211 PD targets, and a Venn analysis found 143 and 220 overlapping targets that plumbago and mitragyana, respectively, might exploit to play pharmacological roles in PD **(Figure 1).**

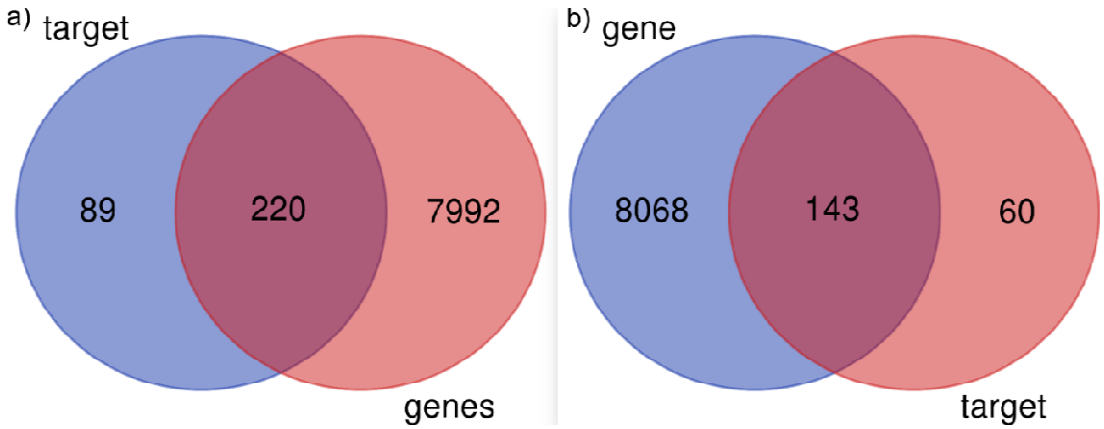

Figure 1. Venn plot for matching each other of gene and target. a) Blue represents targets for mitragyana; red represents for gene of PD. b) Red represents targets for plumbago; blue represents for gene of PD

2.1.2. GO/KEGG analysis results

In ascending order of p-value, we screened the top ten items in the GO and KEGG enrichment analyses. The results of the GO analysis indicate that the biological processes (BP) mainly involve signal transduction, protein phosphorylation, negative regulation of the apoptotic process, one-carbon metabolic process, protein autophosphorylation, response to xenobiotic stimulus, response to the drug, positive regulation of MAP kinase activity, peptidyl-serine phosphorylation, cellular response to cAMP for plumbago plant. Similarly, mitragyana plant BP from GO studies showed, G-protein coupled receptor signaling pathway, coupled to cyclic nucleotide second messenger, positive regulation of ERK1 and ERK2 cascade, chemical synaptic transmission, positive regulation of vasoconstriction. Cell Components include cytosol, cytoplasm, plasma membrane, nucleoplasm, extracellular exosome, membrane raft, perinuclear region of cytoplasm, macromolecular complex, an extrinsic component of cytoplasmic side of the plasma membrane, apical plasma membrane for plumbago, and integral component of plasma membrane, plasma membrane, membrane raft, integral component of presynaptic membrane, presynaptic membrane, synapse, dendrite, neuronal cell body, cytosol, cytoplasm for mitragyana. Molecular functions include carbonate dehydratase activity, hydrolyase activity, enzyme binding, zinc ion binding, protein kinase activity, protein serine/threonine kinase activity, ATP binding, endopeptidase activity, cysteine-type endopeptidase activity

involved in execution phase of apoptosis, identical protein binding for plumbago, and mitragyana for, protein kinase activity, protein serine/threonine kinase activity, ATP binding, transmembrane receptor protein tyrosine kinase activity, identical protein binding, G-protein coupled serotonin receptor activity, carbonate dehydratase activity, protein tyrosine kinase activity, hydro-lyase activity, protein binding **(Supplementary Table S1).**

KEGG analysis demonstrated a total of 83 and 163 pathways with substantial significance (P less than 0.05) for plumbago and mitragyana, respectively. The top ten key pathways for mitragyana were namely Nitrogen metabolism, Cancer pathways, Insulin resistance, Pancreatic cancer, Neuroactive ligand-receptor interaction, Calcium signaling pathway, Sphingolipid signaling pathway, Inflammatory mediator regulation of TRP channels, cAMP signaling pathway, and others. Prostate cancer, Endocrine resistance, Ovarian steroidogenesis, Bladder cancer, Kaposi sarcoma-associated herpesvirus infection, Proteoglycans in cancer, IL-17 signaling pathway, and others are included in plumbago. The two processes that are upstream in other pathways for plumbago and mitragyana, respectively, are the Nitrogen metabolism and Neuroactive ligand-receptor interaction pathways, which have the highest rankings in KEGG **(Supplementary Table S1).**

2.1.3. Network analysis

By constructing the C-T network with Cytoscape 3.9.1, we can look at the connections between the molecules, targets, and pathways of plumbago and mitragyana in more detail. The C-T network, as shown in **Figures 2A for Mitragyana and 2B for Plumbago**, demonstrates interactions between compound targets and pathways. The more important a node is, the greater its degree value. The properties of interactions involving several compounds and targets in Mitragyana and Plumbago are reflected in this network. Additionally, it showed that these substances had a higher potential for bioactivity against PD. In the C-T network, higher degree values for plumbago showed active ingredients as Delphinidin and kaempferol; and in the case of Mitragyana the active ingredients include: Isocorynantheidine, Corynantheidine, Hirsutine, Dihydrocorynantheine, Kaempferol, Corynan, and Dihydrobetahydroxyisomitraphylli. The present analysis suggests a greater likelihood that these natural products may have potential PD -preventing actions **(Figures 2A and 2B).**

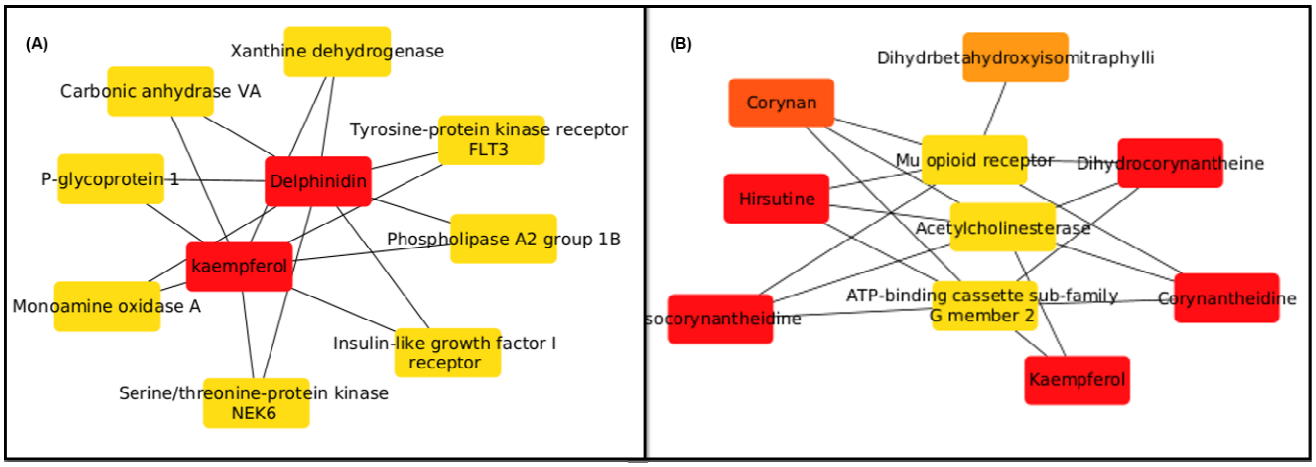

Figure 2. Top ten C-T networks derived from cytoHubba's degree method. (A) Plumbago and (B) Mitragyana plant.

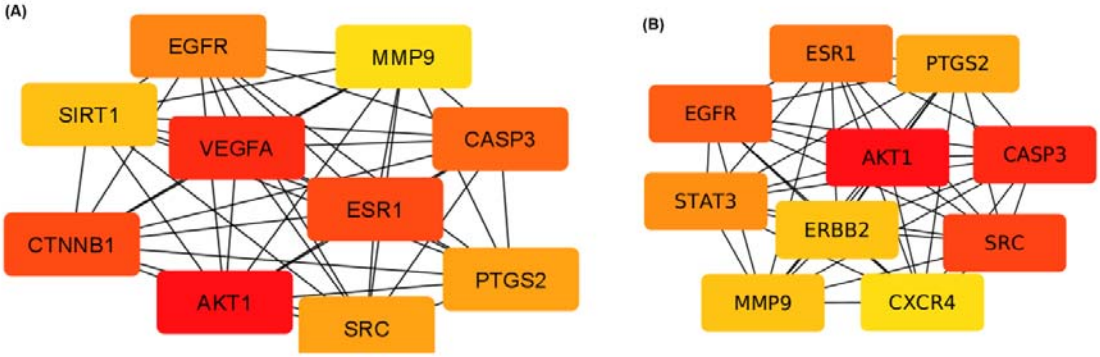

Figure 3. Top ten PPI networks derived from cytoHubba's degree method. (A) Plumbago and (B) Mitragyana plant.

Furthermore, we used the Cytoscape cytohubba plugin to pinpoint significant target proteins in the PPI network. To analyse the important nodes in interaction networks, Cytohubba has access to eleven computational techniques. In addition, the PPI network showed high degree values for plumbago which include: AKT1, VEGFA, CTNNB1, ESR1, CASP3, SRC, PTGS2, EGFR, SIRT1, and MMP9 proteins **(Figure 3A)**. In case of mitragyana, key proteins include AKT1, CASP3, SRC, PTGS2, EGFR, ESR1, STAT3, ERBB2, CXCR4 and MMP9 **(Figure 3B).** AKT1 has a significant function as evidenced by its prominence in the PPI network of both plumbago and mitragyana. In the PPI network, AKT1 has a high score and close connections compared to the other core proteins in the network. We found that AKT1

AKT1 haplotype is comparatively resistant to apoptosis through the p53 pathway is a significant result supporting the protective effect of some haplotypes in this gene against PD. P53 signaling is involved in the death of neurons seen in PD experimental models and causes apoptosis in dopaminergic cells (33-35). AKT1 may be a therapeutic target for PD, according to a significant body of research that has documented its role in the condition. Furthermore, it has been proven through experimentation that mitragyana and plumbago extracts contribute to the Parkinsonism effect [ref]. Thus, the present study suggests that AKT1 was the most significant primary druggable target for PD.

2.2.Machine learning-assisted QSAR study results

Using the ChEMBL web resource client, the ChEMBL database was queried for 4170 inhibitors of AKT1 target and their respective IC_{50} values. After data preprocessing and curation, as well as the eradication of missing values, 3393 compounds were chosen for our study. All 3393 compounds were then subjected to exploratory data analysis which revealed a greater proportion of active compounds than inactive ones. In addition, pIC_{50} values of active compounds ranged from 6.5 to 10, while those of inactive compounds ranged from 3 to 5. The range of LogP values for active compounds was the same as that of inactive compounds. Also, the molecular weight range was greater for active compounds than for inactive compounds. Aside from these, the number of hydrogen bond acceptors was identical for both active and inactive compounds, while the spectrum of hydrogen bond donors was greater for inactive compounds **(Figure 4).**

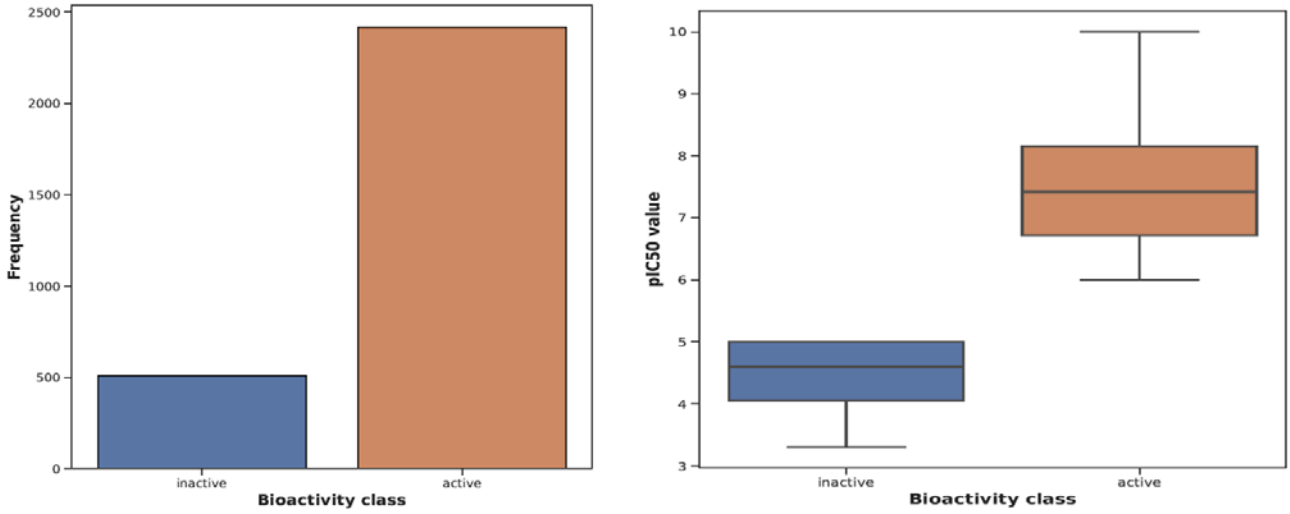

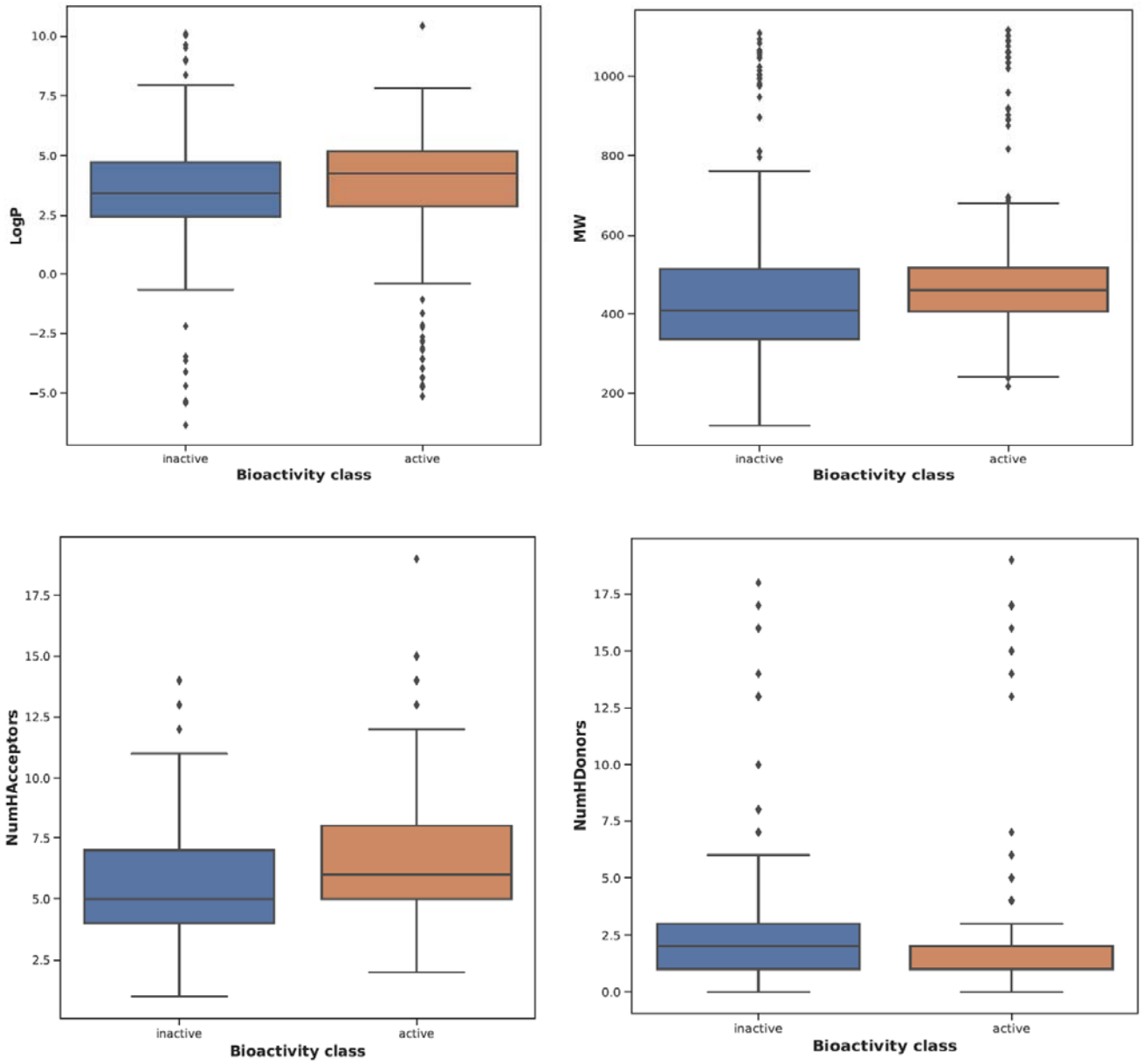

Figure 4: Exploratory data analysis for our AKT1 inhibitors' dataset from the ChEMBL database

The compounds dataset was then subjected to descriptor calculation with PaDELPy of the PaDEL software. Before the implementation of PaDEL, PubChemFP, and SubFP were generated separately. 307 SubPF{attributes were constructed to develop an RF-based QSAR model for the substructure molecular fingerprints. For the development of an additional RF-based QSAR model, an additional 881 PubChem molecular signatures were calculated.

Data pre-treatment GUI 1.2 was then used to eradicate constant descriptors from each dataset based on the correlation threshold score and variance scores. Excluding the biological activity attribute shared by both datasets, the final lists for the PubChem fingerprint (PubChemFP) and substructure fingerprint (SubFP) datasets contain 212 and 22 attributes, respectively. Following the data pretreatment phase, the individual fingerprint datasets were divided using the Kennard Stone algorithm for Dataset division. 80:20 was the

respective split ratio for the training and evaluation sessions. The instruction set consists of 2714 compounds, whereas the test set consists of 679 compounds. To generate the desired QSAR models, the training and test datasets for each descriptor dataset were imported into the machine learning software WEKA.

Comparing the chemical space traversed by the training set (i.e., the 80% subset) to that of the test set (i.e., the 20% subset), the PCA bounding box method was applied to evaluate the applicability domain of the individual molecular fingerprint dataset proposed in this study by detecting outliers for both the fingerprint model. Regarding the PubChemFP dataset, the PCA analysis selected 2589 and 493 molecules for the training and test sets, respectively. Regarding the SubFP dataset, the PCA analysis selected 2201 and 441 molecules for the training and test sets, respectively. Following this, it was discovered that the chemical space spanned by the test set was contained within the chemical space spanned by the training set, and thus was regarded to be within the applicability domain of the developed fingerprint datasets. In addition, the PCA scores diagram **(Figure 5)** reveals that the relative chemical space occupied by compounds in the training and test sets for both the datasets is highly similar.

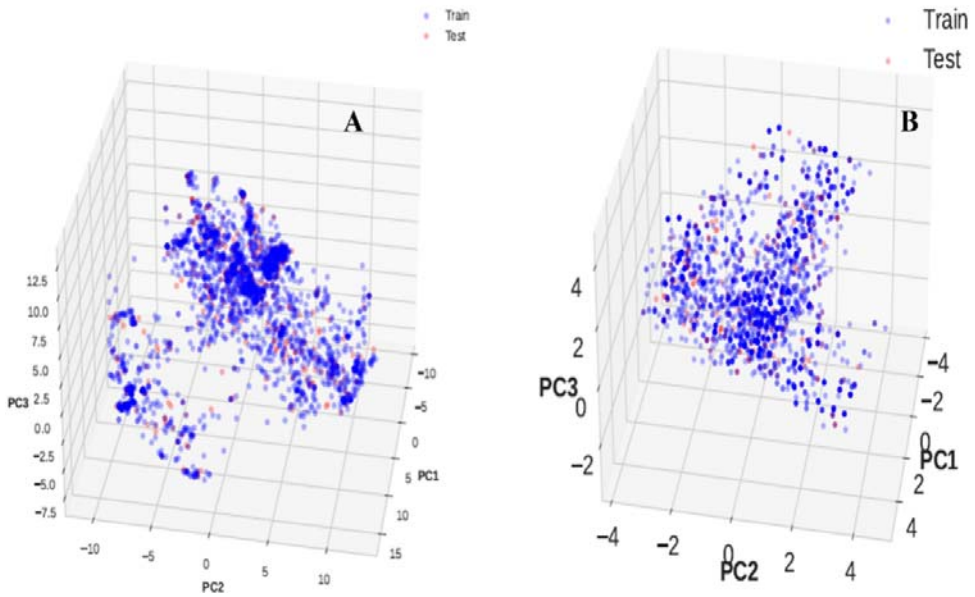

Figure 5: Applicability domain analysis for (A) PubChem fingerprint dataset (B) Substructure fingerprint dataset

Table 1: Statistical metrics and interpretation of PubChemFP and SubFP -based models

Parameters	PubchemFPs training set	PubchemFPs test set	PubchemFPs 10-CV	SubFP training set	SubFP test set	SubFP 10-CV
Correlation coefficient	0.9820	0.9566	0.8662	0.9649	0.9463	0.8720
Kendall's tau	0.8817	0.8025	0.6732	0.8289	0.7856	0.6828
Spearman's rho	0.9809	0.9484	0.8599	0.9606	0.9391	0.8681
Mean absolute error	0.2165	0.3081	0.5287	0.2842	0.3362	0.4941
Root mean	0.2779	0.3764	0.6804	0.3507	0.4049	0.6418

squared error						
Relative absolute error	19.2%	29.5%	46.9%	26.2%	32.7%	45.4%
Root relative squared error	20.7%	29.4%	50.6%	26.9%	32.0%	49.2%
Total Number of Instances	2589	493	2589	2201	441	2201

The correlation coefficient and other statistical parameters were calculated for each fingerprint dataset. The training set correlation coefficient for the PubChem fingerprint dataset was approximately 0.982, while the test set correlation coefficient was 0.9566. It was observed that the root mean squared error (RMSE) for the training set was approximately 0.2779, whereas the RMSE value for the test set was 0.3764. Moreover, the 10-fold cross-validation of the training set data produced a correlation coefficient score of 0.8662. Aside from this, the substructure fingerprint dataset produced correlation coefficients of 0.9649 for the training set and 0.9463 for the test set. It was observed that the root mean squared error (RMSE) for the training set was approximately 0.3507, whereas the RMSE value for the test dataset was 0.4049. In addition, the 10-fold cross-validation of the training set data produced a correlation coefficient score of 0.872%. On the premise of the correlation coefficient between the training and test sets, it was assumed that the QSAR models were highly robust. In addition, the 10-fold cross-validation results for both models were deemed exceptionally satisfactory **(Figures 6, 7, and Table 1).**

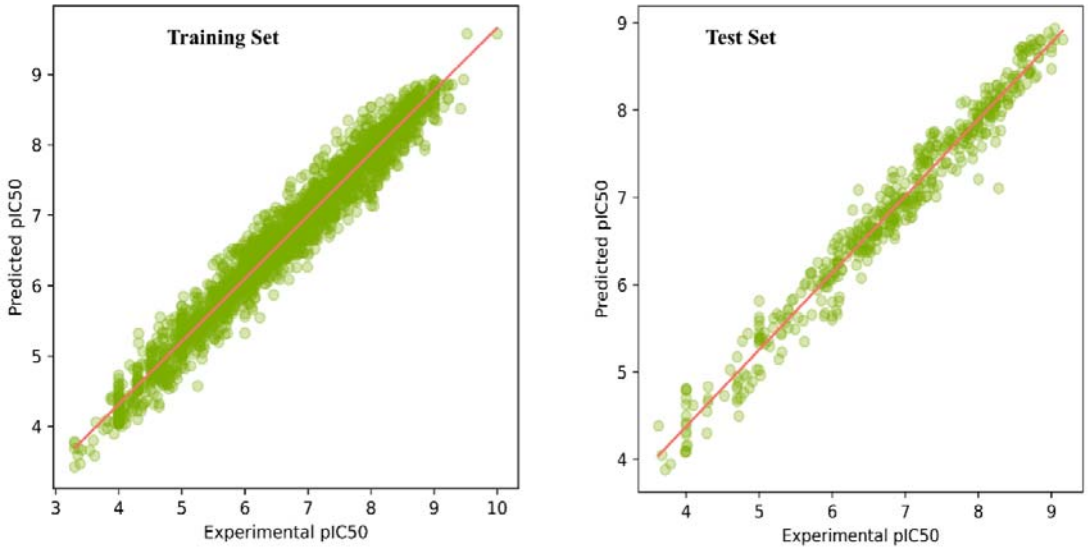

Figure 6: QSAR model scatter plot for PubChem fingerprint dataset

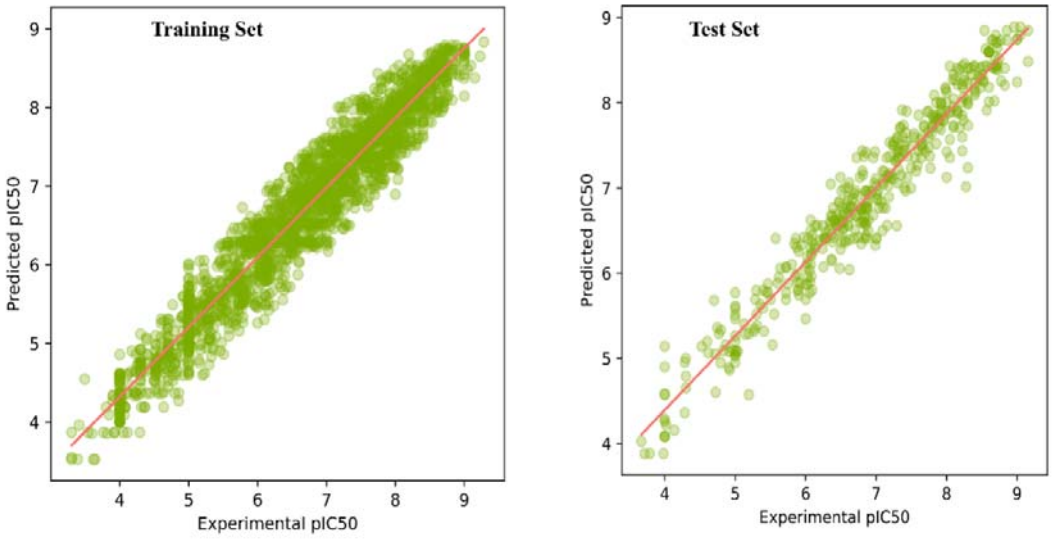

Figure 7: QSAR model scatter plot for substructure fingerprint dataset

Additionally, for each of our QSAR models, a feature importance study was conducted to determine the relevance of individual fingerprints and their contribution to bioactivity. The RF regressor algorithm was utilized to select the top ten molecular fingerprints for every one of our QSAR models. The matplotlib package in Python was used to generate Variance Importance Plots (VIP) for each model's top ten fingerprints. For the PubChemFPs-based model, the VIP plot identified PubchemFPs 129, 335, 338, 374, 392, 438, 477, 521, 696, and 821 as the most significant molecular fingerprints. On the other hand for the SubFPs-based model, the VIP plot identified SubFPs 1, 2, 3, 16, 23, 100, 172, 179, 180, and 181 as the most significant molecular fingerprints **(Figure 8, Table 2).**

Table 2: Interpretation for the most significant PubChemFPs and SubFPs.

Best Features	Interpretation	Best Features	Interpretation
PubchemFP129	>= 1 any ring size 4	SubFP1	Primary carbon
PubchemFP335	C(~C)(~C)(~C)(~H)	SubFP2	Secondary carbon
PubchemFP338	C(~C)(~C)(~H)(~N)	SubFP3	Tertiary carbon
PubchemFP374	C(~H)(~H)(~H)	SubFP16	Dialkylether
PubchemFP392	N(~C)(~C)(~H)	SubFP23	Amine
PubchemFP438	C(-C)(-N)(=N)	SubFP100	Secondary amide
PubchemFP477	C(-H)(=N)	SubFP172	Arylfluoride
PubchemFP521	C(-N)(=O)	SubFP179	Hetero N basic H
PubchemFP696	C-C-C-C-C-C-C-C	SubFP180	Hetero N basic no H
PubchemFP821	CC1C(N)CCCC1	SubFP181	Hetero N nonbasic

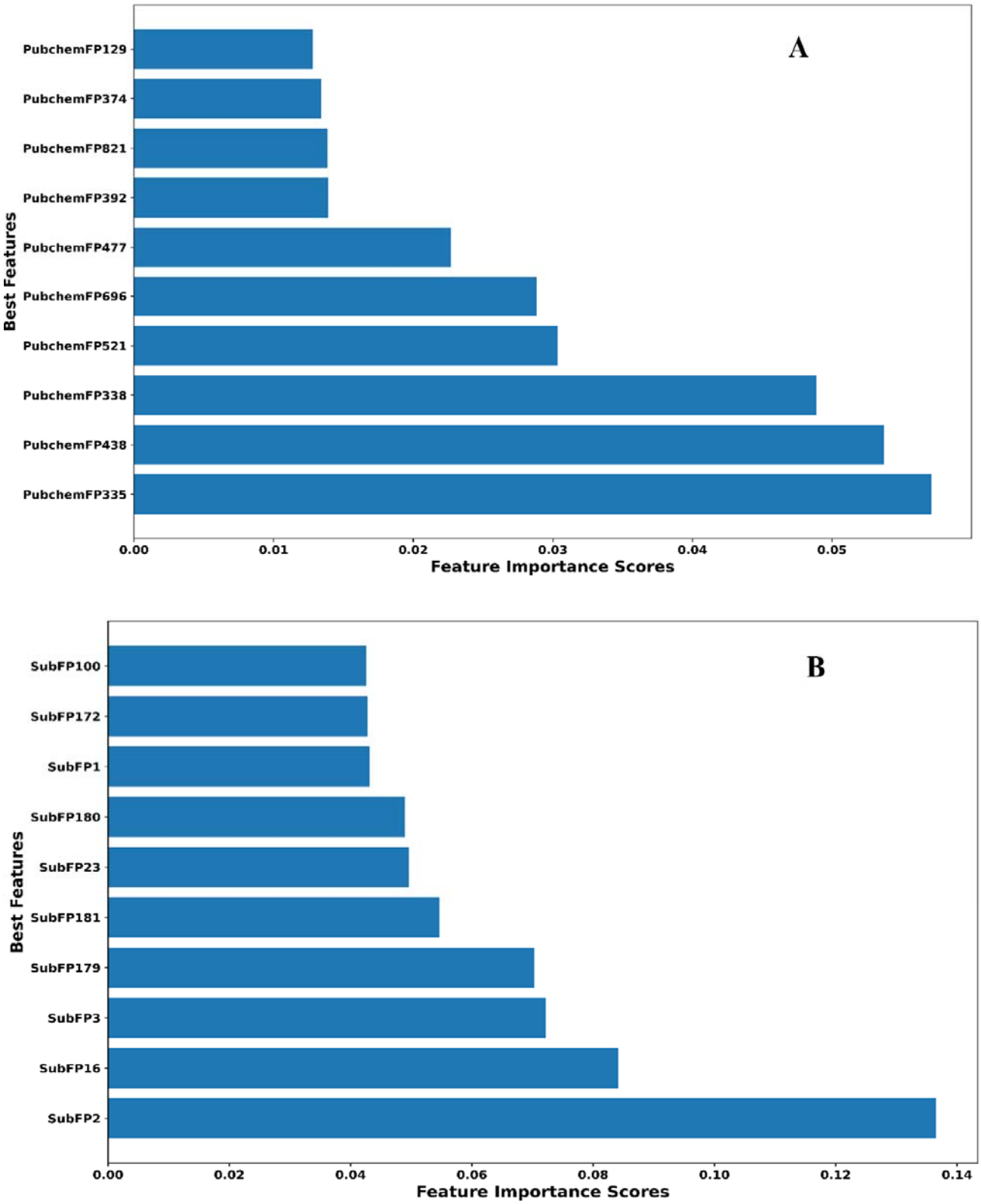

Figure 8: Feature engineering-based variance importance plots for (A) PubChem fingerprint model and (B) Substructure fingerprint model

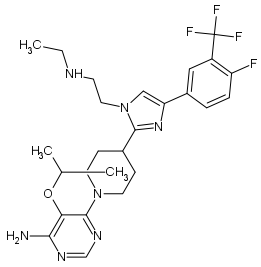

CHEMBL3943127

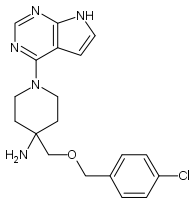

CHEMBL597793

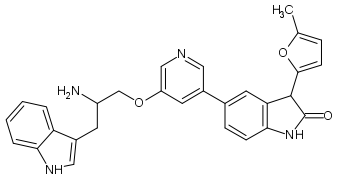

CHEMBL575631

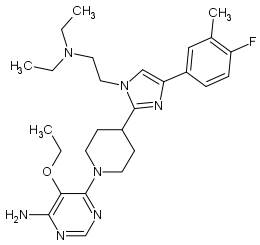

CHEMBL3986943

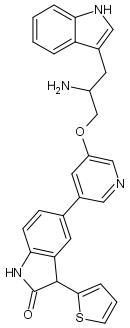

CHEMBL572884

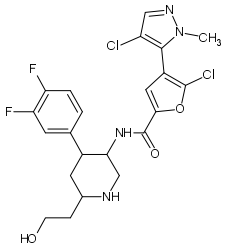

CHEMBL4441825

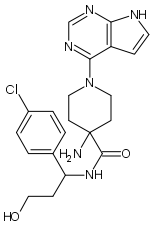

CAPIVASERTIB

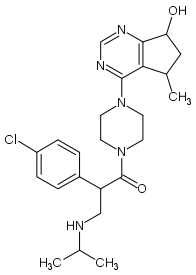

IPATASERTIB

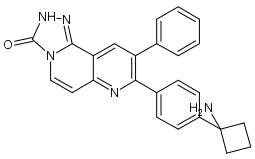

MK-2206

Figure 9: Experimentally tested diverse AKT1 inhibitors.

Based on this molecular feature engineering analysis and VIP plots, a comparison study on the structural insights of the best identified six active molecules obtained from both the models were compared to that of the FDA-approved AKT1 inhibitors. CHEMBL3943127 compound with an experimental pIC_{50} value of 9.284, and predicted pIC_{50} of 8.805 from PubChemFP, and 8.926 from SubFP models respectively, exhibited significant PubchemFPs 335, 374, 392, 438, 521, and 696 along with significant SubFPs 1, 2, 3, 23, 172, 180, and 181 in its chemical structure. CHEMBL597793 compound with an experimental pIC_{50} value of 9.229, and predicted pIC_{50} of 8.544, and 8.695 concerning PubChemFP and SubFP models respectively, exhibited significant PubchemFPs 392, 438, and 521 along with significant SubFPs 2, 16, 179, and 181 in its chemical structure. CHEMBL575631 compound with an experimental pIC_{50} value of 9.155, and predicted pIC_{50} of 8.453, and 8.365 concerning PubChemFP and SubFP models respectively, exhibited significant PubchemFPs 335, 338, 374, 392, 521, 696, and 821 along with significant SubFPs 2, 3, 179, and 181 in its chemical structure. CHEMBL3986943 compound with an experimental pIC_{50} value of 9.097, and predicted pIC_{50} of 8.749, and 8.514 concerning PubChemFP and SubFP models respectively, exhibited significant

PubchemFPs 335, 374, 438, 521, and 696 along with significant SubFPs 1, 2, 3, 23, 172, 180, and 181 in its chemical structure. CHEMBL572884 compound with an experimental pIC50 value of 9.046, and predicted pIC50 of 8.787, and 8.488 concerning PubChemFP and SubFP models respectively, exhibited significant PubchemFPs 335, 338, 392, 521, 696, and 821 along with significant SubFPs 2, 3, 179, and 181 in its chemical structure. CHEMBL441825 compound with an experimental pIC50 value of 9.009, and predicted pIC50 of 8.73, and 8.667 concerning PubChemFP and SubFP models respectively, exhibited significant PubchemFPs 335, 338, 374, 392, 477, 521, and 696 along with significant SubFPs 2, 3, 100, 172, 180, and 181 in its chemical structure.

Concerning FDA-approved AKT1 inhibitors, CHEMBL2325741 (capivasertib) compound with an experimental pIC50 value of 8.523, and predicted pIC50 of 8.431, and 7.979 concerning PubChemFP and SubFP models respectively, exhibited significant PubChemFPs 338, 392, 438, 521 and 696 along with significant SubFPs 2, 100, 179, and 181 in its chemical structure. CHEMBL2325741 (ipatasertib) compound with an experimental pIC50 value of 8.301, and predicted pIC50 of 7.785, and 7.995 concerning PubChemFP and SubFP models respectively, exhibited significant PubchemFPs 335, 338, 374, 392, 438, 521 and 696 along with significant SubFPs 1, 2, 3, 23, and 181 in its chemical structure. CHEMBL2325741 (MK-2206) with an experimental pIC50 value of 8.097, and predicted pIC50 of 7.58, and 8.003 concerning PubChem and substructure fingerprint models respectively, exhibited significant PubchemFPs 129, 438, and 696 along with significant SubFPs 2, and 181 in its chemical structure. Thus, features demonstrated through feature engineering-based VIP plots were found to be significant concerning the key AKT1 inhibitors analyzed **(Figure 9).**

The AUC values for each class, namely active, inactive, and intermediate molecules were 0.99, 1, and 0.97, respectively, based on the ROC plot for the PubChemFP implemented in the QSAR model. Similarly, the AUC values for each class, namely active, inactive, and intermediate molecules were found to be 0.97, 0.96, and 0.92 in the ROC plot for the substructure fingerprints implemented QSAR model. All AUC values for each class for both models were greater than 0.90. These metrics further indicated that the models' performance was significant and dependable **(Figure 10).**

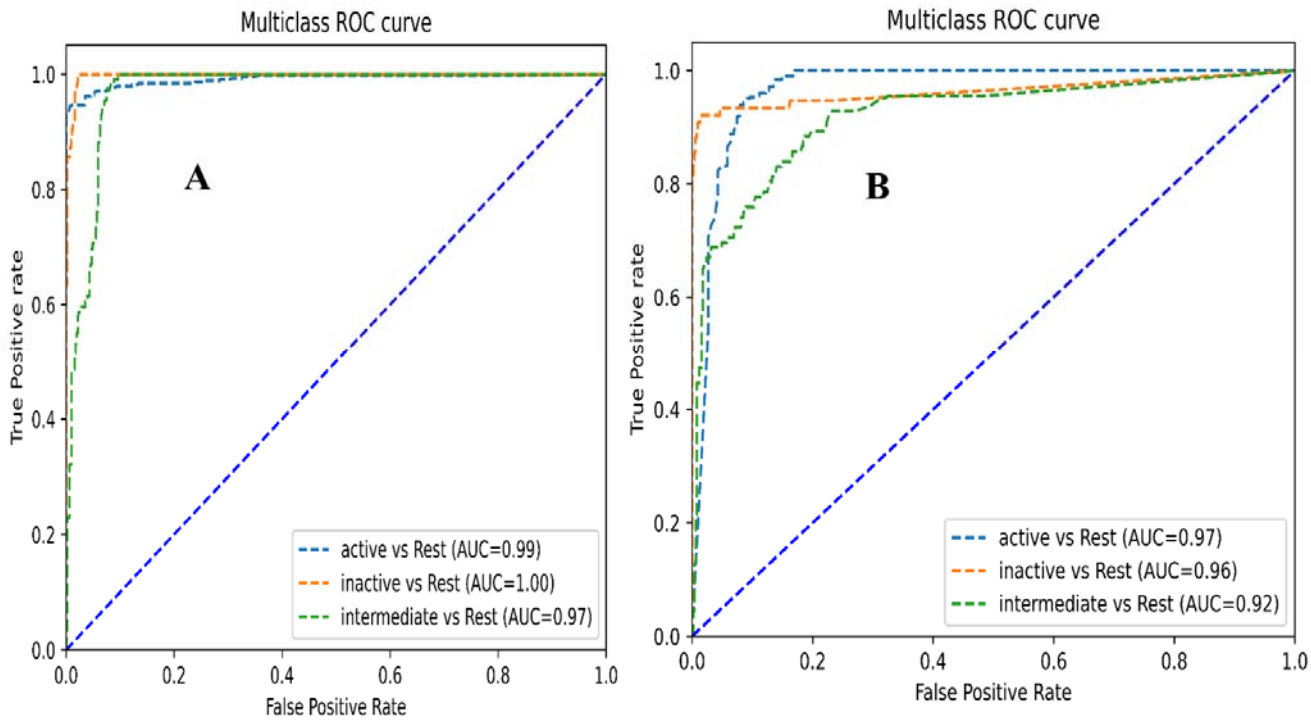

Figure 10: ROC plot for (A) PubChem Fingerprint based model (B) Substructure Fingerprint based model

2.3.Web Application Development

We developed a Python-based web application, named AKT1-Pred (https://akt1pred.streamlit.app/), utilizing the Streamlit library. This application leverages previously established molecular fingerprint-based models for the AKT1 gene. In the process of creating the web application, various Python libraries were employed, including scikit-learn, pandas, subprocess, os, base64, and pickle. AKT1-Pred operates by considering the SMILES representations of multiple molecules, along with their corresponding names or IDs, provided by the user within a text file. Upon uploading this text file containing molecular information, the application conducts predictions for the inhibition activity (pIC_{50}) of the loaded molecules against AKT1. The application employs established fingerprint-based random forest models to calculate the pertinent molecular fingerprints for the loaded molecules. Subsequently, the predicted activity is presented in the form of pIC_{50} values, along with their respective molecule names. Users have the option to download the activity values and molecule names in CSV format directly from the application. The complete source code for AKT1-Pred is openly accessible on GitHub at the following URL: https://github.com/MohanChemoinformaticsLab/Akt1_Pred. To utilize the application on personal workstations, users are required to have the Anaconda Navigator interface installed on their systems, along with Streamlit and other necessary package dependencies. The installation process is detailed in the readme file available on the GitHub repository. By following these instructions, users can accurately predict molecular activity against the AKT1 gene using the AKT1-Pred application.

2.3.1. Prediction of bioactivity of phytochemicals using our generated machine learning models

The phytochemicals identified through screening based on an intensive network pharmacology study were subjected to bioactivity prediction using our generated fingerprint-based machine learning models. Kaempferol, delphinidin, and hirsutine demonstrated the highest bioactivity among all 8 phytochemicals against the AKT1 receptor. Kaempferol demonstrated a pIC_{50} value of 6.2733 and 6.494, delphinidin demonstrated a pIC_{50} value of 6.5107 and 6.246, whereas hirsutine demonstrated a pIC_{50} value of 5.9704 and 6.0484, by PubChemFP and SubFP based machine-learning models respectively (**Table 3**). Following this, the phytochemicals were further subjected to molecular docking and molecular dynamics (MD) simulation study.

Table 3: Predicted activity of phytochemicals using previously generated ML models

Phytochemical	pIC50 PubChemFP model	pIC50 SubFP model
Corynantheidine	5.6100	5.8480
Hirsutine	5.9704	6.0484
Dihydrocorynantheine	5.9897	5.1460
Kaempferol	6.2733	6.4944
Isocorynantheidine	5.2954	5.1465
Corynan	5.2733	5.1460
16,17-Dihydro-17beta-hydroxyisomitraphylline	5.2892	5.6647
Delphinidin	6.5107	6.2460

2.4.Molecular docking and molecular dynamics simulation study

The hit phytochemicals from network pharmacology and the QSAR model were further screened and assessed using the molecular docking technique. Using the Glide module, we docked the successful compounds from the simulated screening into the binding cavity of protein AKT1 having PDB code: 4EKL. Using increased precision (XP), we docked molecules. We also looked at the hits' docking scores, which in XP mode ranged from -4.29 to -8.90 kcal mol-1 (**Table 4**). We re-dock the co-crystalized ligand in the binding site of 4EKL with 1.53 Å RMSD for validating the docking protocol. The top docked hit compounds were delphinidin, and kaempferol with docking scores of −8.90 kcal/mol (XP mode), and −8.30 kcal/mol (XP mode), respectively. The binding affinity of these compounds is comparable with the co-crystalized ligand (Ipatasertib) (XP = −9.40 kcal/mol). All lead compounds bind the same position of co-crystalized ligand of 4EKL. In the binding regions of 4EKL, the chemical delphinidin interacted with important amino acids. These featured the hydrogen-bonding amino acid residues Glu228, Ala230, Asp292, and Glu278 as well as the hydrophobic interactions Tyr229, Met227, Phe438, and Met281. While comparing delphinidin

and kaempferol both show similarities in molecular interactions except Lys172 residue with hydrogen bond **(Table 5 and Figure 11A-11D).**

Table 4. Docking score in XP mode of lead compounds.

Molecule Name	Docking score (XP mode: kcal/mol)
Corynantheidine	-4.29
Hirsutine	-5.34
Dihydrocorynantheine	-5.52
Kaempferol	-8.30
Isocorynantheidine	-5.93
Corynan	-5.44
16,17-Dihydro-17beta-hydroxyisomitraphylline	-5.23
Delphinidin	-8.90
Ipatasertib	-9.40

Table 5. Major interaction lead molecules with AKT1 protein (4EKL).

Sr.No.	Name	Interactions with an amino acid of AKT1 protein
1	Delphinidin	Asp292, Thr291, Glu278, Met281, Glu234, Gly159, Leu156, Val164, Ala230, Tyr229, Glu228, Met227, Ala177, Thr211, Lys172, Phe438
2	Kaempferol	Asp292, Thr291, Glu278, Met281, Glu234, Gly159, Leu156, Val164, Ala230, Tyr229, Glu228, Met227, Ala177, Thr211, Phe438, Lys179
3	Ipatasertib	Asp292, Thr291, Glu278, Met281, Glu234, Gly159, Gly157, Lys158, Gly162, Lys163, Leu156, Val164, Ala230, Tyr229, Glu228, Met227, Ala177, Thr211, Lys172, Lys179, Phe438, Phe442

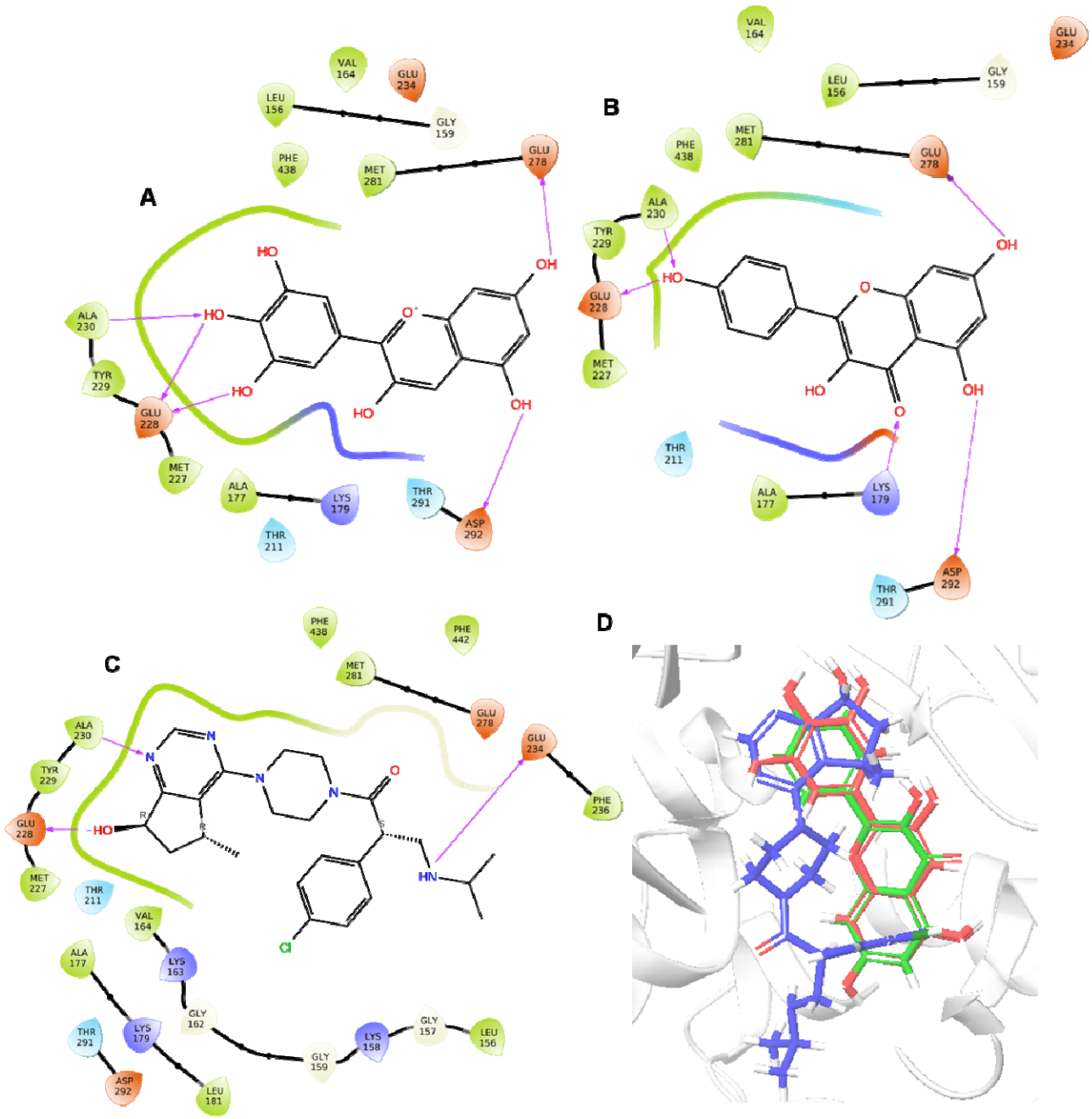

Figure 11. 2D interaction with 4EKL protein. A) delphinidin, B) kaempferol, and C) Ipatasertib. D) Orientation of the lead chemical in a 3D docking pose with the native ligand. Delphinidin, kaempferol, and Ipatasertib are represented by the colors red, green, and blue, respectively.

2.5.Molecular Dynamics Simulation

In the process of computer-aided drug development, MD simulation is a commonly utilized and well-known tool that aids in our understanding of the stability and dynamic interaction of enzyme-ligand complexes. After performing molecular docking against AKT1 (4EKL), we ran 100 ns molecular dynamics (MD) simulations on the delphinidin and kaempferol with the best docking scores (-8.90 and -8.30) and the native ligand (ipatasertib) to assess the stability of the receptor-ligand complex and to compare both the lead

2.5.1. Root Mean Square Deviation (RMSD)

One of the most important indicators to recognize various structural conformations of the protein backbone over time during system equilibration is the root mean square deviation (RMSD) value produced from the MD simulation trajectory. Low and stable RMSD values demonstrate the protein structure's stability. To assess the ligand-protein interaction, the protein should be close to equilibrium, which means that the RMSD value should remain constant. **Figure 12** shows a comparison of the RMSD of both lead and the reference molecule. The alpha carbon atoms in the protein backbone are measured using RMSD, which also assesses protein stability during the simulation. Delphinidin, kaempferol, and ipatasertib had average RMSD values of 2.66±0.25, 2.56±0.28, and 2.53±0.30, respectively. Throughout 100 ns, all of the compounds exhibited behavior that was quite comparable. The only time delphinidin exhibits visual change is for 15 and 55 nanoseconds; otherwise, it is stable, similar to ipatasertib. After 75 ns, a similar steady-state pattern that overlaps with itself has been seen. We can therefore conclude that lead and native chemicals interact with the receptor identically.

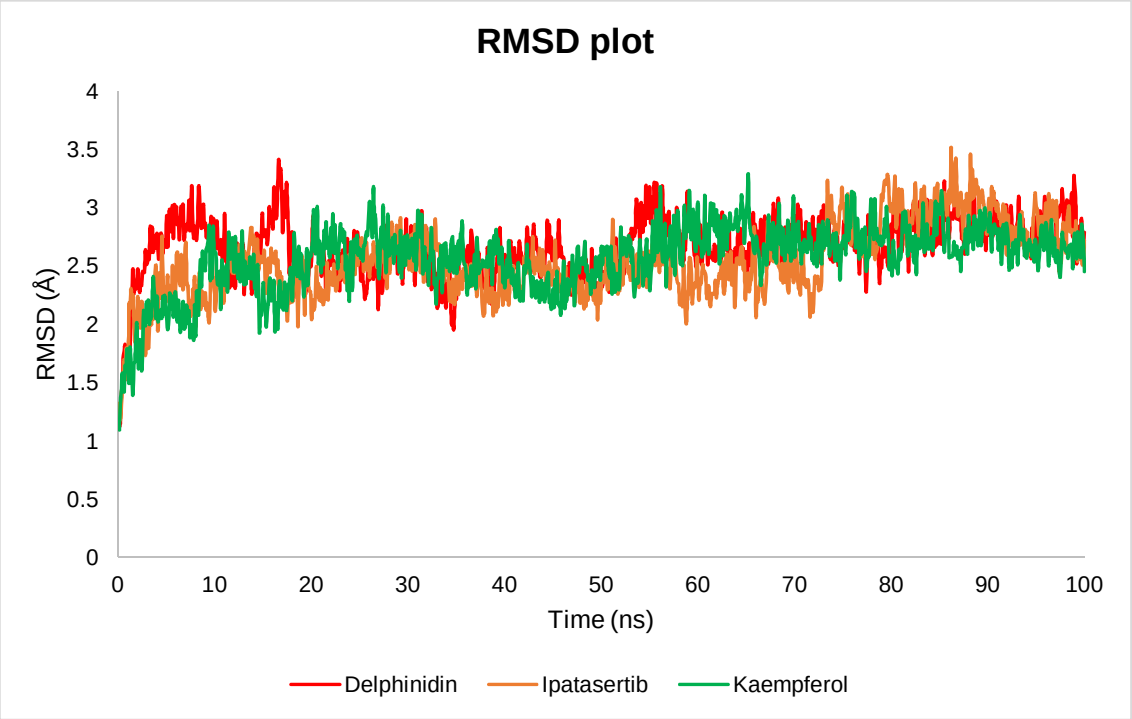

Figure 12. Overlap RMSD plot of delphindin, ipatasertib and kaempferol.

2.5.2. Root mean square fluctuation (RMSF)

The flexibility and mobility of particular amino acids are described by root mean square fluctuation (RMSF) (Figure 13). Given the reduced RMSF, the residue might be less active and mobile. It might be argued that the bond between the protein and ligand is stronger when the RMSF value is low at residues near the active site or at residues where the ligand interacts with the receptor protein. Higher values (peaks) indicated the existence of twists, loose bonding loops, terminal ends, and loose bonding, demonstrating the flexibility of

the structure. Low values indicated secondary structures such as beta sheets, -helices, and alpha helices, which suggested structural stability. The RMSF variation for ipatasertib, kaempferol, and delphinidin with the AKT1 protein was revealed to be 0 0.50-7.47 Å, 0.44-5.12 Å, 0.43-8.28 Å, respectively. By comparing the RMSF values of lead compounds and native ligands, delphinidin, and native ligands exhibit higher fluctuation. When kaempferol was present in the simulation, 20 amino acids showed contacts including, Leu156 (0.71Å), Lys158 (1.36Å), Thr160 (2.49Å), Phe161 (1.76Å), Val164 (0.56Å), Ala177 (0.46Å), Lys179 (0.51Å), Glu198 (0.62Å), Thr211 (0.71Å), Glu228 (0.56Å), Ala230 (0.55Å), Glu234 (0.61Å), Lys276 (0.60Å), Glu278 (0.75Å), Asn279 (0.71Å), Met281 (0.56Å), Thr291 (0.60), Asp292 (0.61Å), Phe293 (0.59Å), and Phe438 (0.89Å). In case of delphindin Lys158 (1.10Å), Thr160 (1.76Å), Phe161 (2.63Å), Val164 (0.65Å), Ala177 (0.52Å), Lys179 (0.52Å), Thr211 (0.65Å), Met227 (0.52Å), Glu228 (0.58Å), Ala230 (0.57Å), Glu234 (0.66Å), Lys276 (0.63Å), Glu278 (0.76Å), Asn279 (0.62Å), Met281 (0.53Å), Thr291 (0.56), Asp292 (0.56Å), and Phe442 (1.20Å). Except for Phe442 and Met227 for delphinidin and Lys156, Phe293, and Phe438 for kaempferol, both lead molecules and native ligands with almost identical amino acids demonstrated interaction during the simulation, with very minor RMSF variation.

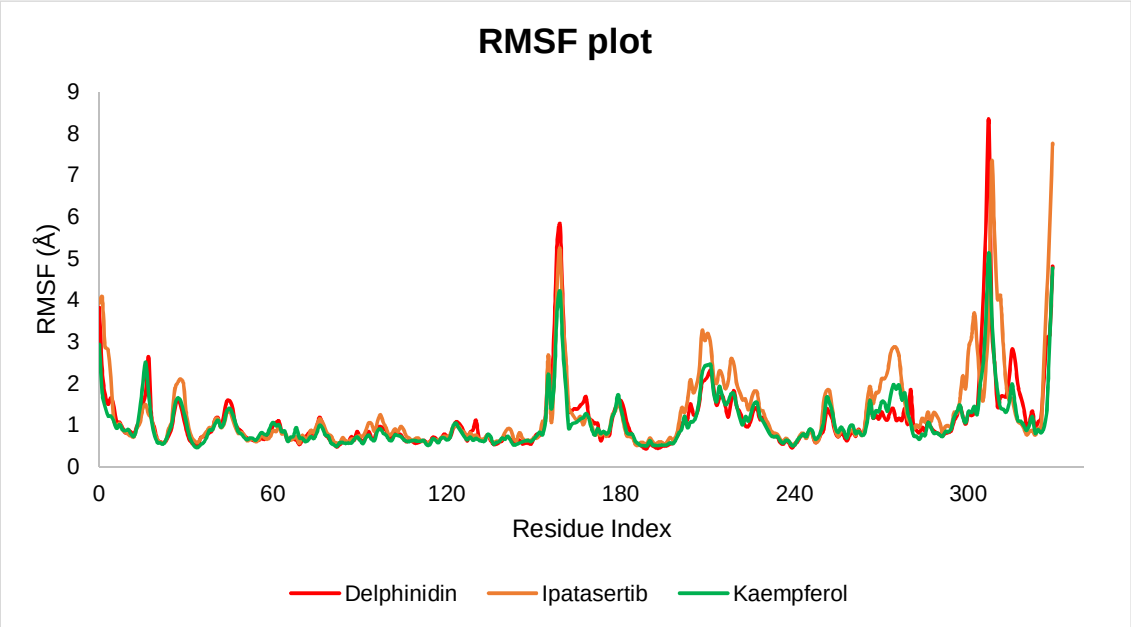

Figure 13. Overlap RMSF plot of delphindin, ipatasertib, and kaempferol.

2.5.3. Protein-ligand Contact

Hydrogen bonding is an essential element of drug design that helps in comprehending the metabolism, adsorption, and specificity of a drug candidate. The significant contribution of non-covalent interactions, such as hydrophobic interactions, π-Cation; π-π; polar or ionic interactions, and the formation of a water-bridge hydrogen bond, also helped to clarify how docked protein-ligand poses evolved throughout the MD simulation period. **Figures 14A-14C** show how lead molecules and native ligands bind together when the

4EKL protein's binding pocket contains active-site amino acid residues. Hydrophobic contacts, hydrogen bonds, and polar (water-mediated hydrogen bonding) binding make up the majority of significant interactions between chemicals and proteins that MD simulations have revealed. However, the important amino acids for the AKT1 binding site are Glu228, Ala230, Glu234, Val164, Glu278, Thr291, and Asp292 residues. These interlocking residues were also visible in the corresponding docked complexes **(Table 5, Figure 11A-11C)**, which indicates that docked ligands remained in the active pocket throughout the simulation. According to studies of the protein-ligand contact mapping, certain bioactive compounds significantly dwell in the catalytic pocket of AKT1 as compared to the native molecule. This allows for marking of the bioactive components in descending sequence from ipatasertib. Kaempferol and delphinidin were found to be effective AKT1 inhibitors based on the number of molecular interactions created during the 100 ns MD simulation duration.

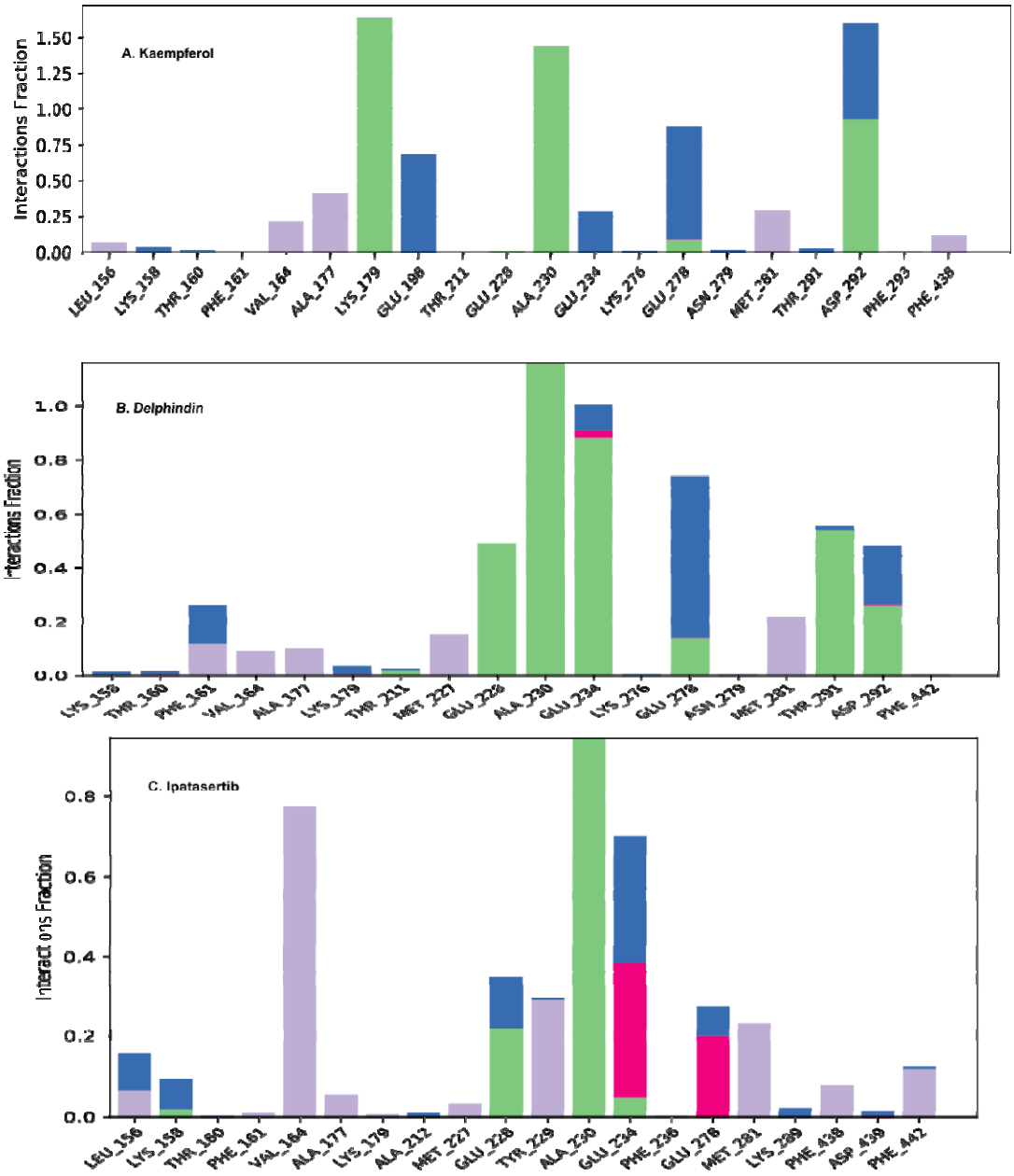

Figure 14. Protein−ligand contact histogram analysis. Red (ionic), green (hydrogen bond), blue (water bridge), and grey (hydrophobic) are represented by color in the histogram. A) Kaempferol B) Delphindin C) Ipatasetib.

3. Conclusion

In this study, network pharmacology was used to screen possible active natural plants including Mitragyna Speciosa and Plumbago Indica. This study used network integration analysis to pinpoint AKT1 as the main target for PD therapy. The 2-dimensional QSAR model that was created using the PubChemFP and SubFP is also included. As the most important molecular fingerprints, PubChemFPs 129, 335, 338, 374, 392, 438, 477, 521, 696, and 821 and SubFPs 1, 2, 3, 16, 23, 100, 172, 179, 180, and 181 were identified. Additionally, delphinidin and kaempferol compounds were found to be extremely effective AKT1 inhibitors. The active drugs' stable binding to AKT1 active site residues were further supported by the molecular docking outcomes. Additionally, MD simulations showed that delphinidin and kaempferol are stable in dynamic systems, and when compared to ipatasertib (the natural ligand), it was clear that both lead compounds have a strong affinity for AKT1. For the benefit of the scientific community, the fingerprint-based predictive models were further deployed as the AKT1-Pred web server (https://akt1pred.streamlit.app/) and the source codes and data sets were made available on GitHub (https://github.com/MohanChemoinformaticsLab/Akt1_Pred) to encourage further extension or modification of the web server. It is important to observe that, as new experimental data on small molecule-based AKT1 inhibitors become available, the predictive model proposed here could be continuously updated to increase its coverage and accuracy. The results of our *in-silico* investigation may provide new understanding of the molecular pathways that prevent PD from progressing and suggest prospective treatment drugs. Further pharmacodynamic and pharmacological research will be done on the best chemicals to see how they work to treat PD.

4. Materials and Methods

4.1.Network pharmacology

4.1.1. Chemical compounds and targets acquisition

To find the chemical components in Plumbago indica and Mitragyna speciosa, we use the KNapSAcK (http://www.knapsackfamily.com/knapsack_core/top.php) and the Indian Medicinal Plants, Phytochemistry and Therapeutic (IMPPAT) databases. The OB value (Oral bioavailability), DL value (Drug-likeness), and probability for the target are 30%, 18%, and 0.1 as reference points for filter compounds. The PubChem database's SDF version of their structures was obtained. Then we used SwissTargetPrediction (http://www.swisstargetprediction.ch/) to find compound targets, entered "Parkinson's disease" into GeneCards and OMIM to find genes associated with PD (score>30), and then analyzed the intersection

targets with the help of the Venny2.1.0 platform to find the proper targets of plumbago and mitragyana against PD.

4.1.2. GO/KEGG analysis

DAVID Bioinformatics Resources (https://david.ncifcrf.gov/home.jsp) is a well-known bioinformatics resource system for functional annotation and enrichment analysis of gene lists [26]. The intersecting targets of plumbago and mitragyna therapy for PD were uploaded to the DAVID database after we chose Homo sapiens as the species, inserted data from Gene Ontology (GO) and the Kyoto Encyclopaedia of Genes and Genomes (KEGG). Biological processes are annotated, and signaling pathways of important targets are examined.

4.2.3. C-T and PPI network construction

The interactions between compounds, targets, and pathways are widely studied using the "Compounds-Targets" (C-T) network [27]. Additionally, by methodically examining and identifying key targets, the analysis of Protein-protein Interaction (PPI) networks can help us comprehend the molecular mechanisms underlying disease [28]. The STRING database (https:// string-db.org/) was used to obtain the PPI network. Using the Cytoscape 3.9.1 program, we constructed the C-T network and ranked chemicals according to degree value to estimate their relevance. The analysis of the cytohubba plugin in Cytoscape 3.9.1 was used to look at the main targets in the PPI network.

4.2.Machine Learning Assisted QSAR Study

4.2.1. Data curation and Pre-processing

A query search of the ChEMBL database for AKT1 inhibitors with potency measured in nanomolar (nM) units comprised the initial phase. Using Lipinski's rule of five descriptors (molecular weight, ALogP, hydrogen bond donor, and hydrogen bond acceptor), exploratory data analysis or chemical space analysis was done to explore the chemical space of the inhibitory compounds. Based on their AKT 1 inhibitory action, the virtually screened (VS) ChEMBL compounds were further divided into three categories: active, inactive, or intermediate. Compounds with activity values below 1000 nM were deemed active, while those with activity values between 1,000 and 10,000 nM were deemed intermediate, and those with activity values above 10,000 nM were deemed inactive.

4.2.2. Molecular Descriptor Calculation

Our research made use of the PaDELPy module (bash script) of the PaDEL software to calculate various molecular fingerprints for the ChEMBL compound dataset we had previously acquired. In our research for

the Random Forest-based machine learning algorithm, we utilized the PaDEL software to incorporate PubChem and substructure molecular fingerprints. To conduct a comprehensive structural analysis of previously identified PDL-1 inhibitors, two distinct types of molecular fingerprints were used to construct two different QSAR models. Substructure fingerprint descriptors of PaDEL software were used to obtain insights regarding functional groups of each chemical structure, while PubChem fingerprints were used to evaluate the significance of atomic indices regarding each small molecule in our ChEMBL dataset. A user-defined variance cut-off value was used to identify relevant descriptors in the ChEMBL dataset, and constant descriptors with the same or nearly the same values for all compounds were eliminated. The user-specified inter-correlation coefficient cut-off value was used to identify and process inter-correlated descriptors similarly. The ChEMBL dataset was split 80:20 between training and test sets using the final best AKT1 inhibitor and the Kennington Stone algorithm.

4.2.3. Development and Validation of Random forest-based QSAR models

Using the aforementioned ChEMBL (AKT1) datasets, Random Forest (RF)-based machine learning models were created using Weka Tool. RF is a technique for supervised machine learning consisting of a collection or ensemble of predictors based on basic decision trees. The Bagging or Bootstrap aggregation technique is used to train RF. Additionally; this approach makes an effort to address the overfitting problem seen in decision trees. The QSAR models were then validated by comparing the correlation coefficient (R^2) between the training dataset and the validation dataset. The best molecular features could be chosen by implementing the RF Regressor algorithms for the RF models and showing them as Variance Importance Plots (VIP). The experimental versus predicted values for each QSAR model were contrasted graphically using the matplotlib Python package[36, 37].

Moreover, receiver operating characteristics (ROC) graphs were constructed for both QSAR models using a built-in Python script based on multiclass model classification. The ROC is a graphical tool for evaluating classifier performance and monitoring the performance of classification-based QSAR models using features produced by confusion matrices. Comparison of the true positive (TP) rate and the false positive (FP) rate on a scale from 0 to 1. The area under the curve (AUC) has been devised as a quantitative metric for ROC analysis competitive evaluation. The AUC of a ROC plot is a reliable estimate of the efficacy of a discriminant model. Its value ranges from 0 to 1 (total misclassification to perfect classification). The applicability domain (AD) of both QSAR models was also evaluated using the bounding box method of principal component analysis (PCA). This requires a PCA analysis of the scores plot to compare the chemical space of training and test set molecules. AD was carried out in Python using the PCA function from the sklearn.decomposition module of the scikit-learn machine learning framework.

4.2.4. Molecular Docking Study

The three-dimensional (3D) crystal structure of AKT1 (PDB ID: 4EKL, Resolution: 2.0 Å) [29] was meticulously selected and retrieved from the Protein Data Bank (PDB) (http://www.rcsb.org). Before

selecting the PDB ID, we conducted a thorough literature evaluation. Using this PDB, Maestro can integrate a workflow. By removing water molecules, altering side chain protonation states, and adding lacking hydrogen, the crystal structures were optimized and minimized using the Protein Preparation Wizard program. After the initial preparation steps, the essential protein was further processed to produce the grid. Building a receptor grid around the co-crystallized ligand (Ipatasertib) of the enzyme enabled researchers to identify the binding site. Using the LigPrep module and the OPLS-2005 force field, the compounds were prepared for Glide docking [30,31, 38].

4.2.5. Molecular Dynamics Simulation Study

For the MD studies for the lowest docking pose of the compound Apo and the co-crystallized ligand with 4EKL using the OPLS-2005 force field, the Desmond package (Desmond V 7.2) was installed on a Dell Inc. precision 7820 Tower with the configuration Ubuntu 22.04.1 LTS 64-bit, Intel Xenon (R) silver 4210R, and NVIDIA Corporation GP104GL (RTX A 4000) graphics processing unit[32]. The MD system box specs were an orthorhombic box form and a 5× 5× 5 $Å^3$ buffer capacity. Explicit water molecules (TIP4P) were used to set up the MD system, then 0.15 M NaCl ion concentrations were introduced to neutralize the system. NPT ensembles were used in MD simulations for Nose-Hoover temperature coupling at 310 K and Martyna-Tobias-Klein pressure coupling at 1.01 bar constant pressure. During the 100ns MD simulation, an analysis of the RMSD, RMSF, and protein-ligand interaction was constructed to assess the domain correlations. Following the MD run, 1000 frames were created for each MD trajectory at 100ps intervals to study the binding kinetics of protein-ligand interaction [30, 31. 38].

Data Availability

The machine-learning guided bioactivity prediction model-based web application against AKT1 is available at: https://akt1pred.streamlit.app/ .

Acknowledgements

The authors thank the Finnish Cultural Foundation, Tampere Tuberculosis Foundation, Academy of Finland, and Jane and Aatos Erkko Foundation for financial support for this study.

Conflicts of interest

The authors have no conflicts of interest.

Reference

(1) Zhang, H.; Bai, L.; He, J.; Zhong, L.; Duan, X.; Ouyang, L.; Zhu, Y.; Wang, T.; Zhang, Y.; Shi, J. Recent Advances in Discovery and Development of Natural Products as Source for Anti-Parkinson's Disease Lead Compounds. *Eur. J. Med. Chem.* **2017**, *141*, 257–272.

(2) Kapoor, S.; Bourdoumis, A.; Mambu, L.; Barua, J. Effective Management of Lower Urinary Tract Dysfunction in Idiopathic P Arkinson's Disease. *Int. J. Urol.* **2013**, *20* (1), 79–84.

(3) Jankovic, J.; Lang, A. E. Diagnosis and Assessment of Parkinson Disease and Other Movement Disorders. *Bradley's Neurol. Clin. Pract. E-b.* **2021**, *310* (1).

(4) Grammatopoulos, T. N.; Jones, S. M.; Ahmadi, F. A.; Hoover, B. R.; Snell, L. D.; Skoch, J.; Jhaveri, V. V; Poczobutt, A. M.; Weyhenmeyer, J. A.; Zawada, W. M. Angiotensin Type 1 Receptor Antagonist Losartan, Reduces MPTP-Induced Degeneration of Dopaminergic Neurons in Substantia Nigra. *Mol. Neurodegener.* **2007**, *2*, 1–17.

(5) Winter, C.; von Rumohr, A.; Mundt, A.; Petrus, D.; Klein, J.; Lee, T.; Morgenstern, R.; Kupsch, A.; Juckel, G. Lesions of Dopaminergic Neurons in the Substantia Nigra Pars Compacta and in the Ventral Tegmental Area Enhance Depressive-like Behavior in Rats. *Behav. Brain Res.* **2007**, *184* (2), 133–141.

(6) BK, B.; Bal, A.; Kandimalla, R. J. L.; Gill, K. D. Nigrostriatal Neuronal Death Following Chronic Dichlorvos Exposure: Crosstalk between Mitochondrial Impairments, α Synuclein Aggregation, Oxidative Damage and Behavioral Changes. *Mol. Brain* **2010**, *3* (1), 1–20.

(7) Wong, Y. C.; Luk, K.; Purtell, K.; Burke Nanni, S.; Stoessl, A. J.; Trudeau, L.; Yue, Z.; Krainc, D.; Oertel, W.; Obeso, J. A. Neuronal Vulnerability in Parkinson Disease: Should the Focus Be on Axons and Synaptic Terminals? *Mov. Disord.* **2019**, *34* (10), 1406–1422.

(8) Binde, C. D.; Tvete, I. F.; Gåsemyr, J. I.; Natvig, B.; Klemp, M. Comparative Effectiveness of Dopamine Agonists and Monoamine Oxidase Type-B Inhibitors for Parkinson's Disease: A Multiple Treatment Comparison Meta-Analysis. *Eur. J. Clin. Pharmacol.* **2020**, *76*, 1731–1743.

(9) Oertel, W.; Schulz, J. B. Current and Experimental Treatments of Parkinson Disease: A Guide for Neuroscientists. *J. Neurochem.* **2016**, *139*, 325–337.

(10) Heim, M. D.; Eva-Maria Hametner, M. D.; Atbin Djamshidian-Tehrani, M. D.; Regina Katzenschlager, M. D.; Shen-Yang Lim, M. D.; Santiago Perez Lloret, M. D.; Cristina Sampaio, M. D.; Susan, H.; Daniel Weintraub, M. D. International Parkinson and Movement Disorder Society Evidence-Based Medicine Review: Update on Treatments for the Non-Motor Symptoms of Parkinson's Disease. **2018**.

(11) Huang, C.; Zhang, Z.; Cui, W. Marine-Derived Natural Compounds for the Treatment of Parkinson's Disease. *Mar. Drugs* **2019**, *17* (4), 221.

(12) Vo, T. N. N.; Frei, K.; Truong, D. D. Guidelines for the Use of Parkinsonian Drugs (in USA). *NeuroPsychopharmacotherapy* **2020**, 1–21.

(13) E Adkins, J.; W Boyer, E.; R McCurdy, C. Mitragyna Speciosa, a Psychoactive Tree from Southeast Asia with Opioid Activity. *Curr. Top. Med. Chem.* **2011**, *11* (9), 1165–1175.

(14) Warner, M. L.; Kaufman, N. C.; Grundmann, O. The Pharmacology and Toxicology of Kratom: From Traditional Herb to Drug of Abuse. *Int. J. Legal Med.* **2016**, *130* (October), 127–138.

(15) Singh, D.; Müller, C. P.; Murugaiyah, V.; Hamid, S. B. S.; Vicknasingam, B. K.; Avery, B.; Chear, N. J. Y.; Mansor, S. M. Evaluating the Hematological and Clinical-Chemistry Parameters of Kratom (Mitragyna Speciosa) Users in Malaysia. *J. Ethnopharmacol.* **2018**, *214* (March), 197–206.

(16) Li, S.; Cunningham, A. B.; Shi, Y.; Qiu, Z.; Hartl, A.; Ding, X.; Wu, S.; Wang, Y. Blue to Black: Hypotheses on Plant Use Complexity in Traditional Dyeing Processes in Southeast Asia and China. *Ind. Crops Prod.* **2022**, *188* (November), 115706.

(17) Saha, R.; Chakravorty, A.; Kumari, A.; Gupta, K.; Sarkar, N.; Chakraborty, M. Assessment of Anti-Seizure Property of Plumbago Indica L. on Zebrafish Model. *Eur. J. Pharm. Res.* **2023**, *3* (2), 1–4.

(18) Li, J.; Li, J.-X.; Jiang, H.; Li, M.; Chen, L.; Wang, Y.-Y.; Wang, L.; Zhang, N.; Guo, H.-Z.; Ma, K.-L. Phytochemistry and Biological Activities of Corynanthe Alkaloids. *Phytochemistry* **2023**, *213*, 113786.

(19) Veeramohan, R.; Zamani, A. I.; Azizan, K. A.; Goh, H.-H.; Aizat, W. M.; Razak, M. F. A.; Yusof, N. S. M.; Mansor, S. M.; Baharum, S. N.; Ng, C. L. Comparative Metabolomics Analysis Reveals Alkaloid Repertoires in Young and Mature Mitragyna Speciosa (Korth.) Havil. Leaves. *PLoS One* **2023**, *18* (3), e0283147.

(20) Ishikawa, H. Collective Synthesis of Monoterpenoid Indole Alkaloids Using Bioinspired Strategies. In *New Tide of Natural Product Chemistry*; Springer, 2023; pp 211–234.

(21) Qu, J.; Lu, J.; Hu, Y. Research and Development of Anti-Parkinson's Drugs: An Analysis from the Perspective of Technology Flows Measured by Patent Citations. *Expert Opin. Ther. Pat.* **2019**, *29* (2), 127–135.

(22) Zhang, H.; Tong, R.; Bai, L.; Shi, J.; Ouyang, L. Emerging Targets and New Small Molecule Therapies in Parkinson's Disease Treatment. *Bioorg. Med. Chem.* **2016**, *24* (7), 1419–1430.

(23) Tang, Z.; Li, L.; Xia, Z. Exploring Anti-Nonalcoholic Fatty Liver Disease Mechanism of Gardeniae Fructus by Network Pharmacology, Molecular Docking, and Experiment Validation. *ACS omega* **2022**, *7* (29), 25521–25531.

(24) Hu, Y.; Wu, Y.; Jiang, C.; Wang, Z.; Shen, C.; Zhu, Z.; Li, H.; Zeng, Q.; Xue, Y.; Wang, Y.

Investigative on the Molecular Mechanism of Licorice Flavonoids Anti-Melanoma by Network Pharmacology, 3D/2D-QSAR, Molecular Docking, and Molecular Dynamics Simulation. *Front. Chem.* **2022**, *10*, 843970.

(25) Chen, P.-Y.; Han, L.-T. Study on the Molecular Mechanism of Anti-Liver Cancer Effect of Evodiae Fructus by Network Pharmacology and QSAR Model. *Front. Chem.* **2023**, *10*, 1060500.

(26) Sherman, B. T.; Hao, M.; Qiu, J.; Jiao, X.; Baseler, M. W.; Lane, H. C.; Imamichi, T.; Chang, W. DAVID: A Web Server for Functional Enrichment Analysis and Functional Annotation of Gene Lists (2021 Update). *Nucleic Acids Res.* **2022**, *50* (W1), W216–W221.

(27) Chen, P.; Yuan, C.; Hong, Z.; Zhang, Y.; Ke, X.; Yu, B.; Wang, C.; Xiao, X.; Wu, H.; Yang, Y. Revealing the Mechanism of "Huai Hua San" in the Treatment of Ulcerative Colitis Based on Network Pharmacology and Experimental Study. *J. Ethnopharmacol.* **2021**, *281*, 114321.

(28) O'Reilly, M.; Cleasby, A.; Davies, T. G.; Hall, R. J.; Ludlow, R. F.; Murray, C. W.; Tisi, D.; Jhoti, H. Crystallographic Screening Using Ultra-Low-Molecular-Weight Ligands to Guide Drug Design. *Drug Discov. Today* **2019**, *24* (5), 1081–1086.

(29) Lin, K.; Lin, J.; Wu, W.-I.; Ballard, J.; Lee, B. B.; Gloor, S. L.; Vigers, G. P. A.; Morales, T. H.; Friedman, L. S.; Skelton, N. An ATP-Site on-off Switch That Restricts Phosphatase Accessibility of Akt. *Sci. Signal.* **2012**, *5* (223), ra37–ra37.

(30) Eduardo Sanabria-Chanaga, E.; Betancourt-Conde, I.; Hernández-Campos, A.; Téllez-Valencia, A.; Castillo, R. In Silico Hit Optimization toward AKT Inhibition: Fragment-Based Approach, Molecular Docking and Molecular Dynamics Study. *J. Biomol. Struct. Dyn.* **2019**, *37* (16), 4301–4311.

(31) Kumar, S., Jayan, J., Manoharan, A., Benny, F., Abdelgawad, M.A., Ghoneim, M.M., El-Sherbiny, M., Thazhathuveedu Sudevan, S., Aneesh, T.P. and Mathew, B. Discerning of isatin-based monoamine oxidase (MAO) inhibitors for neurodegenerative disorders by exploiting 2D, 3D-QSAR modelling and molecular dynamics simulation. *J. Biomol. Struct. Dyn.* **2023**, pp.1-13..

(32) Maestro-Release, D. Desmond Molecular Dynamics System, Maestro-Desmond Interoperability Tools. *Shaw Res.* **2017**.

(33) Harris, S. L.; Gil, G.; Robins, H.; Hu, W.; Hirshfield, K.; Bond, E.; Bond, G.; Levine, A. J. Detection of Functional Single-Nucleotide Polymorphisms That Affect Apoptosis. *Proc. Natl. Acad. Sci.* **2005**, *102* (45), 16297–16302.

(34) Nair, V. D. Activation of P53 Signaling Initiates Apoptotic Death in a Cellular Model of Parkinson's Disease. *Apoptosis* **2006**, *11* (6), 955–966.

(35) Duan, W.; Zhu, X.; Ladenheim, B.; Yu, Q.; Guo, Z.; Oyler, J.; Cutler, R. G.; Cadet, J. L.; Greig, N. H.; Mattson, M. P. P53 Inhibitors Preserve Dopamine Neurons and Motor Function in Experimental

Parkinsonism. *Ann. Neurol. Off. J. Am. Neurol. Assoc. Child Neurol. Soc.* **2002**, *52* (5), 597–606.

(36) Melge, A.R., Parate, S., Pavithran, K., Koyakutty, M. and Mohan, C.G. Discovery of Anticancer Hybrid Molecules by Supervised Machine Learning Models and in Vitro Validation in Drug Resistant Chronic Myeloid Leukemia Cells. *J. Chem Inf. Model.*. **2022**, *62*(4), pp.1126-1146.

(37) Kuttappan, Shruthy, Ratul Bhowmik, and C. Gopi Mohan. Probing the origins of programmed death ligand-1 inhibition by implementing machine learning-assisted sequential virtual screening techniques. *Mol. Divers.* **2023**, 1-18.

(38) Kumar, S., Manoharan, A., Jayalakshmi, J., Abdelgawad, M.A., Mahdi, W.A., Alshehri, S., Ghoneim, M.M., Pappachen, L.K., Zachariah, S.M., Aneesh, T.P. and Mathew, B., 2023. Exploiting butyrylcholinesterase inhibitors through a combined 3-D pharmacophore modeling, QSAR, molecular docking, and molecular dynamics investigation. *RSC Adv*. **2023**, *13*(14), pp.9513-9529.
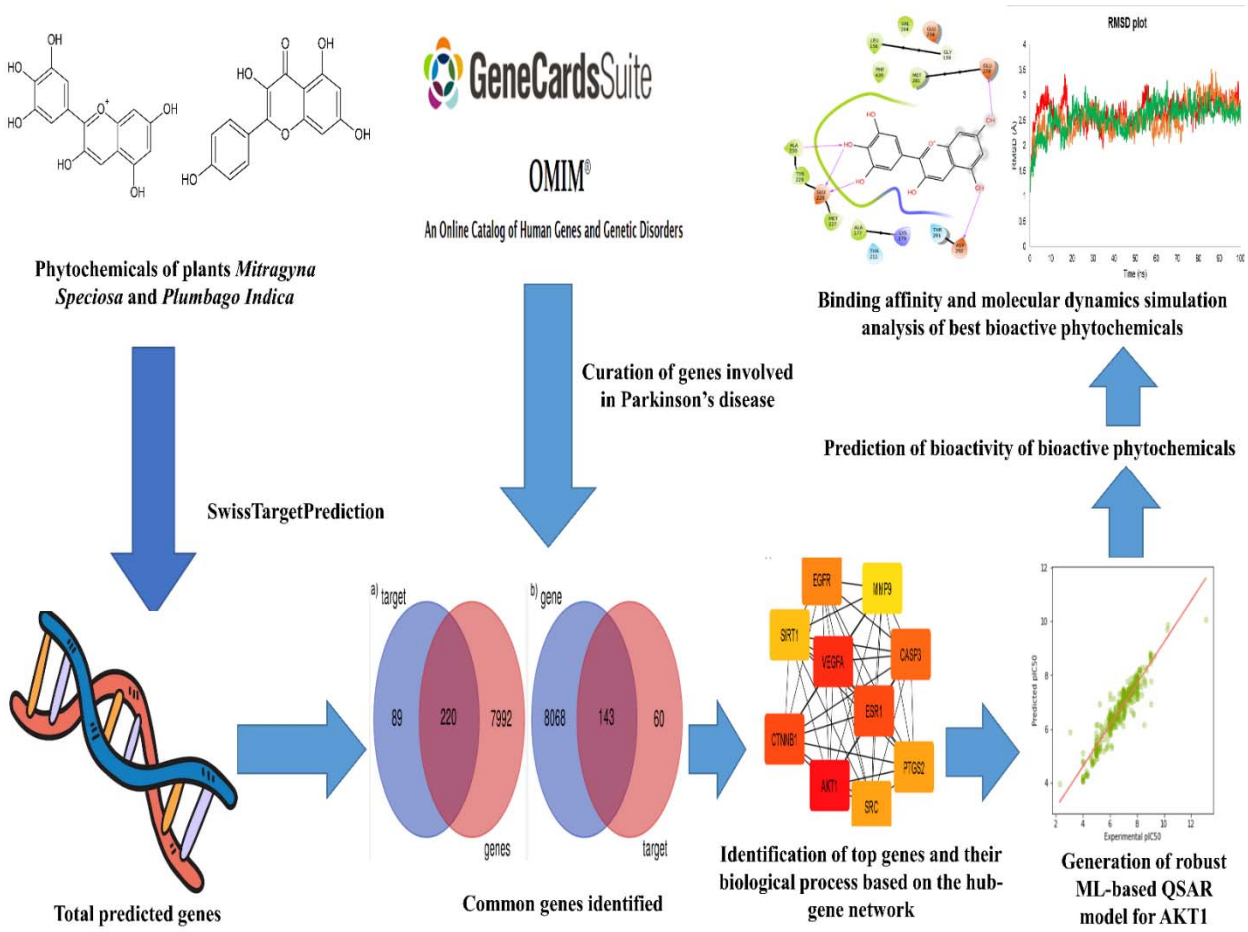
Graphical Abstract